Syntheses, Characterisation, and Computational Studies of Tungsten Hexafluoride Adducts with Pyridine and Its Derivatives

Douglas Turnbull[a,b], Nathan Kostiuk[a,b], Stacey D. Wetmore[a,b], and Michael Gerken[*a,b]

[a]Canadian Centre for Research in Advanced Fluorine Technologies and [b]Department of Chemistry and Biochemistry, University of Lethbridge, 4401 University Drive W, Lethbridge, AB, CA T1K 3M4

[*]Corresponding author. Tel.: +1-403-329-2173; Fax: +1-403-329-2057; E-mail address: michael.gerken@uleth.ca.

Congratulations to Erhard Kemnitz on receiving the 2018 ACS Award for Creative Work in Fluorine Chemistry

Abstract

The reactions of WF_6 with pyridine, 4-methylpyridine, 4-(dimethylamino)pyridine, and 4'4-bipyridine (4,4′-bipy) in CH_2Cl_2 afford the Lewis-acid-base adducts $WF_6(4\text{-}NC_5H_4R)$ (R = H, CH_3, $N(CH_3)_2$) and $F_6W(4,4'\text{-bipy})WF_6$ as solids in quantitative yields. These adducts have been characterised in the solid state by Raman spectroscopy at ambient temperature and, in the cases of the mononuclear adducts, by X-ray crystallography at –173 °C. Furthermore, density-functional-theory (DFT-B3LYP) studies have been conducted to aid in predicting the structure of $F_6W(4,4'\text{-bipy})WF_6$, assigning the vibrational frequencies of the adducts, and comparing their electronic properties.

Keywords

Tungsten hexafluoride, Lewis-acid-base adduct, Heptacoordinate, Crystal structure

1. Introduction

The transition-metal hexafluorides, MF_6 (M = Mo, Tc, Ru, Rh, W, Re, Os, Ir, Pt), are expected to behave as moderate Lewis acids, with calculated fluoride-ion affinities ranging from 264 (M = Rh) to 345 (M = Os) kJ mol^{-1},[1,2] the latter being comparable to that of BF_3 (344 kJ mol^{-1}).[3] However, salts of the homoleptic $[MF_7]^-$ or $[MF_8]^{2-}$ anions have only been isolated and conclusively characterised for the hexafluorides of groups 6 and 7.[4,5] Molski and Seppelt have postulated that this is due to either the lower charge on the metal centres of the group 8–10 hexafluorides, or their partially filled *d* orbitals, either of which would serve to preclude bonding interactions between the metal centre and incoming fluorido ligand.[4]

Furthermore, WF_6 is the only transition-metal hexafluoride for which there exists definitive evidence of Lewis-acid behaviour towards organic Lewis bases. The reactions of WF_6 with $Pn(CH_3)_3$ (Pn = N, P) and pyridine resulted in the formation of solid Lewis-acid-base adducts,

formulated as $WF_6\{Pn(CH_3)_3\}$ and $WF_6(NC_5H_5)_n$ (n = 1, 2), which were characterised by ^{19}F NMR spectroscopy.[6] The ^{19}F NMR spectra of these adducts consisted of broad singlets, with the exception of a broad doublet produced by $WF_6\{P(CH_3)_3\}$ due to $^2J(^{19}F–^{31}P)$ coupling, which were attributed to the six fluorido ligands undergoing rapid exchange in solution. Fluorine-19 NMR spectroscopic studies of mixtures of WF_6 and $S(CH_3)_2$ revealed that $WF_6\{S(CH_3)_2\}$ still undergoes rapid intramolecular ligand exchange at –75 °C (further cooling results in precipitation from the vinyl chloride solvent) whereas $WF_6\{S(CH_3)_2\}_2$ adopts a rigid bicapped trigonal-prismatic structure at –160 °C, with the sulfido ligands occupying the capping positions (though this was not deduced in the original article).[7] It was later determined by low-temperature ^{19}F NMR spectroscopy that the $WF_6(NC_5H_5)_n$ adducts adopt monocapped (n = 1) and bicapped (n = 2) trigonal-prismatic geometries in solution.[8] The similarities between the ^{19}F NMR spectra of $WF_6(NC_5H_5)_2$ and $WF_6\{S(CH_3)_2\}_2$ suggest that they share a common geometry.

Due to the fluxional nature of the adducts, especially those that are heptacoordinate, in solution on the NMR timescale, X-ray crystallography has been more commonly used to assess their geometries. The ambient-temperature crystal structures of $WF_6(2\text{-}NC_5H_4F)$ [9] and $WF_6(NC_5H_5)_2$ [8] revealed mono- and bicapped-trigonal-prismatic geometries for the adducts, respectively. Interestingly, it was determined that, although $WF_6\{P(CH_3)_3\}$ adopts the same geometry as the nitrogen-base adducts,[10] $WF_6\{P(C_6H_5)(CH_3)_2\}$ prefers the monocapped-octahedral ligand arrangement observed for the anions in $Cs[WF_7]$[11] and $Cs[WF_6(OCH_2CF_3)]$.[12] This illustrates the marginal differences in energy between the monocapped-octahedral and monocapped-trigonal-prismatic geometries, as well as the dependence of the resultant geometry on the chosen ligand. These geometries are also similar in

energy to the third model heptacoordinate geometry, the pentagonal bipyramid, which has not yet been observed for any neutral or anionic derivative of WF_6.

The reaction of 2,2′-bipyridine (2,2′-bipy) with a molar equivalent of WF_6 is reported to result in WF_6(2,2′-bipy),[13] which is also afforded upon dismutation of WOF_4(2,2′-bipy), with WO_2F_2(2,2′-bipy) being formed as a by-product.[14] However, if WF_6 is present in a large molar excess, ligand-induced autoionisation occurs and $[WF_4(2,2'\text{-bipy})_2]^{2+}$ salts are obtained in which the cation adopts a dodecahedral geometry.[13,15]

Such complexes have mostly found application as involatile sources of WF_6. The $[NF_4][WF_7]$ salt has been prepared as a generator of NF_3, F_2, and WF_6 gases,[16] whereas [Emim][WF_7] (Emim = 1-ethyl-3-methylimidazolium) is an ionic liquid with a melting point (−15 °C) that is lower than the analogous BF_4^- and MF_6^- (M = P, As, Sb, Nb, Ta) salts.[17] In addition, we have recently demonstrated the utility of $WF_6(NC_5H_5)$ and $[N(CH_3)_4][WF_7]$ as synthetic equivalents to WF_6 in facile syntheses of $[W(NC_6F_5)F_5]^-$ salts.[18]

Herein, the syntheses and structural characterisation of heptacoordinate WF_6 adducts with 4-methylpyridine and 4-(dimethylamino)pyridine, as well as a dinuclear 2:1 adduct with 4,4′-bipyridine, are detailed. In addition, the crystal structure of $WF_6(NC_5H_5)$ was elucidated. Complementary DFT (B3LYP) studies have been conducted, and the effects of ligand basicity on structure and bonding in Lewis-acid-base adducts of WF_6 are discussed.

2. Results and Discussion

2.1. Syntheses and Properties of WF_6(4-NC_5H_4R) (R = H, CH_3, $N(CH_3)_2$) and F_6W(4,4′-bipy)WF_6

The WF_6(4-NC_5H_4R) (R = H, CH_3, $N(CH_3)_2$) and F_6W(4,4′-bipy)WF_6 adducts are conveniently prepared by the reaction of the corresponding pyridine derivative with an excess of WF_6 in CH_2Cl_2 at ambient temperature (Equations 1 and 2), as described previously for

$WF_6(NC_5H_5)$.[8] Upon removal of the solvent and excess WF_6 under dynamic vacuum up to ambient temperature, the adducts are obtained as fine white powders, with the exception of WF_6{4-$NC_5H_4N(CH_3)_2$}, which instead has an intense red-orange colour. The mononuclear adducts are soluble to varying degrees, in CH_3CN, CH_2Cl_2, and SO_2, whereas F_6W(4,4′-bipy)WF_6 is insoluble in these solvents.

$$WF_6 + 4\text{-}NC_5H_4R \xrightarrow{CH_2Cl_2} WF_6(4\text{-}NC_5H_4R);\ R = H,\ CH_3,\ N(CH_3)_2 \quad (1)$$

$$2WF_6 + 4,4'\text{-bipy} \xrightarrow{CH_2Cl_2} F_6W(4,4'\text{-bipy})WF_6 \quad (2)$$

The pyridine and 4-methylpyridine adducts have been found to volatilise slowly *in vacuo* at room temperature, and as such can only be held under such conditions for brief periods. Although $WF_6(NC_5H_5)$ is seemingly indefinitely stable if stored under an inert atmosphere of N_2, it appears to slowly sublime over extended periods without decomposition, whereas WF_6(4-$NC_5H_4CH_3$) decomposes within weeks in the solid state at ambient temperature, or hours in CH_3CN, to afford a brown material. The adducts are highly reactive towards traces of moisture and HF, leading to cleavage of the W–F and W–N bonds, respectively (Equations 3 and 4). Because HF is formed as a hydrolysis product, it is typical to simultaneously observe traces of both impurities in the sample.

$$WF_6(B) + H_2O \rightarrow WOF_4(B) + 2HF \quad (3)$$

$$WF_6(B) + HF \rightarrow [BH][WF_7] \quad (4)$$

Attempts to synthesise $WF_6(NC_5H_5)$ in CH_3CN invariably resulted in contamination of the product with an unidentified brown material, signalling the occurrence of side reactions. However, if the excess WF_6 is removed before the introduction of CH_3CN, no such side reactions occur. Thus, it appears that the WF_6-CH_3CN system is a stronger oxidant than WF_6 alone and is capable of oxidising the nitrogen bases employed in this study. The enhanced oxidising capabilities of WF_6

in the presence of CH_3CN have been observed previously in its reactions with iron[19] and tungsten,[20] which do not typically proceed under mild conditions. Analogous reactions performed in SO_2 resulted in increased contamination by WOF_4 derivatives, which is attributed to fluorine-oxygen exchange between WF_6 and SO_2, because similar side reactions have been previously observed.[21]

$$WF_6 + SO_2 \rightarrow WOF_4 + SOF_2 \quad (5)$$

2.2. Molecular Geometries

The solid-state structures of $WF_6(4\text{-}NC_5H_4R)$ (R = H, CH_3, $N(CH_3)_2$) were elucidated by X-ray crystallography at –173 °C. In addition, gas-phase geometries were optimised for these adducts along with $F_6W(4,4'\text{-bipy})WF_6$ and previously reported $WF_6(2\text{-}NC_5H_4F)$ using the experimental geometries of the adducts as starting points whenever possible. Crystallographic data collection and refinement parameters are provided in Table 1. Selected experimental and calculated geometric parameters are given in Table 2; complete geometric parameters are provided in the Supporting Information (Tables S1–S4).

Table 1. Crystallographic Data Collection and Refinement Parameters for $WF_6(4\text{-}NC_5H_4R)$ (R = H, CH_3, $N(CH_3)_2$)

	R = H	**R = CH_3**	**R = $N(CH_3)_2$**
Chemical formula	$C_5H_5F_6NW$	$C_6H_7F_6NW$	$C_7H_{10}N_2F_6W$
Formula weight	376.95	390.98	421.03
Temperature (°C)	–173	–173	–173
Crystal system	triclinic	monoclinic	monoclinic
Space group	$P\bar{1}$	$P2_1/n$	$C2/c$
a (Å)	6.8162(3)	9.0570(4)	11.4523(5)
b (Å)	7.9414(3)	8.7114(3)	12.2477(5)
c(Å)	8.0005(3)	11.5124(4)	7.7085(3)
α (°)	70.630(4)		
β (°)	81.142(4)	97.253(3)	108.970(5)
γ (°)	78.213(3)		
V (Å$^{3)}$	398.19(3)	901.05(6)	1022.50(8)
Z	2	4	4
R_1 [I ≥ 2σ(I)][a]	0.0360	0.0208	0.0131
wR_2 [I ≥ 2σ(I)][b]	0.0927	0.0483	0.0307
CCDC	1853269	1853270	1853271

[a] $R_1 = \sum||F_o| - |F_c||/\sum|F_o|$. [b] $wR_2 = [\sum[w(F_o^2 - F_c^2)^2]/\sum w(F_o^4)]^{1/2}$.

Table 2. Selected Experimental and Calculated Bond Lengths (Å) and Angles (°) in $WF_6(4\text{-}NC_5H_4R)$ (R = H, CH_3, (R = H, CH_3, $N(CH_3)_2$) and $F_6W(4,4'\text{-bipy})WF_6$

	$WF_6(NC_5H_5)$		$WF_6(4\text{-}NC_5H_4CH_3)$		$F_6W(4,4'\text{-bipy})WF_6$		$WF_6\{4\text{-}NC_5H_4N(CH_3)_2\}^c$		
	exptl	calcd[a]	exptl	calcd[a]	calcd[b] θ = 0.2°	calcd[b] θ = 89.9°		exptl	calcd[a]
W–F(1)	1.880(6)	1.868	1.875(2)	1.868	1.867	1.866	W–F(1)	1.8711(14)	1.873
W–F(2)	1.875(5)	1.868	1.868(2)	1.868	1.867	1.866			
W–F(3)	1.861(5)	1.877	1.859(2)	1.878	1.878	1.879	W–F(2)	1.8696(14)	1.880
W–F(4)	1.864(5)	1.877	1.858(2)	1.878	1.878	1.879	W–F(3)	1.8628(14)	1.880
W–F(5)	1.843(5)	1.877	1.858(2)	1.878	1.878	1.879			
W–F(6)	1.868(5)	1.877	1.867(2)	1.878	1.878	1.879			
W–N	2.251(7)	2.343	2.250(3)	2.339	2.351	2.357	W–N(1)	2.214(3)	2.301
F(1)–W–F(2)	75.1(3)	76.3	75.70(10)	76.3	76.5	76.6	F(1)–W–F(1)^i	75.49(9)	76.2
F(1)–W–F(3)	77.4(2)	79.3	78.94(11)	79.2	79.5	79.5	F(1)–W–F(2)	77.69(7)	78.9
F(1)–W–F(4)	124.1(3)	127.8	126.35(11)	127.4	128.1	127.9	F(1)–W–F(3)	124.96(7)	127.3
F(3)–W–F(4)	81.6(3)	80.5	80.53(11)	80.1	80.5	79.9	F(2)–W–F(3)	81.36(6)	80.7
F(3)–W–F(5)	90.5(3)	90.9	91.72(10)	91.7	90.7	91.4	F(2)–W–F(3)^i	91.77(6)	91.4
F(3)–W–F(6)	149.6(2)	148.4	151.21(10)	149.0	148.9	148.3	F(2)–W–F(2)^i	150.86(10)	149.6
F(1)–W–N	143.2(3)	141.9	143.20(10)	141.8	141.8	141.7	F(1)–W–N(1)	142.25(5)	142.0
F(3)–W–N	74.8(3)	74.2	75.74(11)	74.5	73.9	74.1	F(2)–W–N(1)	75.43(5)	74.8
F(1)–W–N–C(1)	–3.6(9)	0.0	90.0(3)	90.0	0.2	89.9	F(1)–W–N(1)–C(1)^i	3.3(2)	0.0

[a]Calculated using the B3LYP functional with the Stuttgart basis set augmented by one f-type polarisation function (W; $\alpha_f = 0.823$) and the aug-cc-pVTZ (H, C, N, F) basis set. [b]Calculated using the B3LYP functional with the Stuttgart basis set augmented by one f-type polarisation function (W; $\alpha_f = 0.823$) and the cc-pVTZ (H, C, N, F) basis set. Theta (θ) is defined as the F(1)–W–N–C(1) dihedral angle. [c]Symmetry transformation *i*: 1–x, +y, 1.5–z.

The $WF_6(NC_5H_5)$ adduct crystallises in the triclinic space group $P\bar{1}$, whereas its methyl and dimethylamino derivatives crystallise in the monoclinic space groups $P2_1/n$ and $C2/c$, respectively. The compounds manifest as discrete molecular entities with no significant intermolecular contacts. In the pyridine and 4-methylpyridine adducts, all atoms are crystallographically unique, whereas in $WF_6\{4\text{-}NC_5H_4N(CH_3)_2\}$, the molecule lies on a twofold axis and possesses crystallographically imposed C_2 symmetry.

The adducts adopt monocapped-trigonal-prismatic geometries with the pyridyl ligands in the capping positions (Fig. 1), resulting in approximately C_{2v}-symmetric structures. Interestingly, $WF_6(4\text{-}NC_5H_4CH_3)$ adopts a geometry in which the plane of the pyridyl ligand is orthogonal to the opposing edge of the trigonal prism formed by F(1) and F(2), resulting in a F(1)–W–N–C(1) dihedral angle (θ) of 90.0(3)°. This contrasts with the other adducts, which are structurally similar to $WF_6(2\text{-}NC_5H_4F)$ ($\theta \approx 0°$).[9] The invariant observation of a monocapped-trigonal-prismatic geometry in these complexes, despite significant differences in the BF_3 affinities (i.e., Lewis basicities) of 2-fluoropyridine (97 kJ mol^{-1}), pyridine (128 kJ mol^{-1}), 4-methylpyridine (134 kJ mol^{-1}), and 4-(dimethylamino)pyridine (152 kJ mol^{-1}),[22] suggest that the geometry best assuages the steric demands of the pyridyl ligand. However, even 4-(dimethylamino)pyridine is a significantly weaker Lewis base than "naked fluoride", which instead yields a monocapped-octahedral geometry in the $[WF_7]^-$ anion.[11]

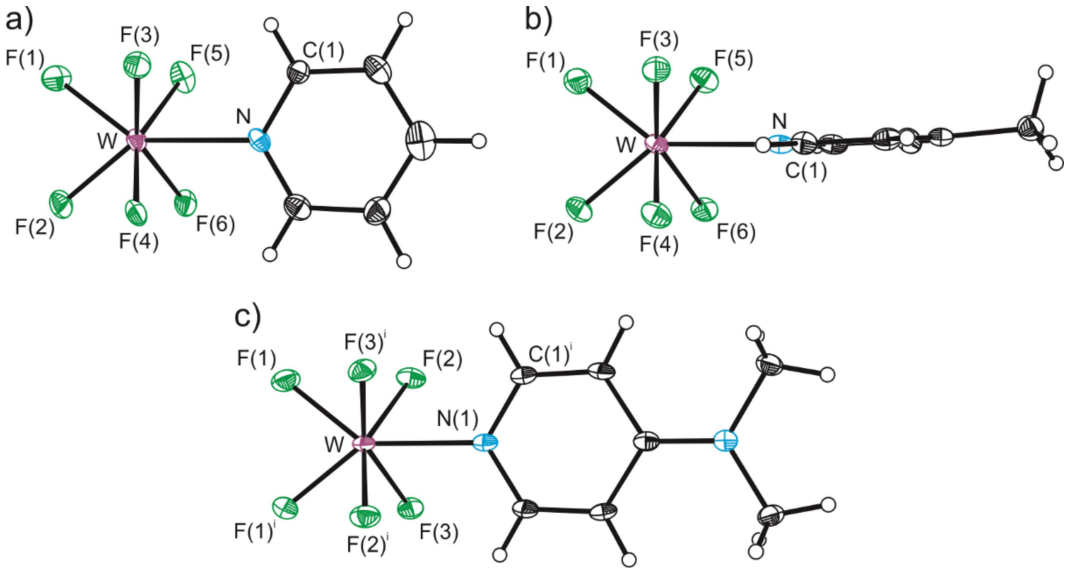

Fig. 1. Thermal ellipsoid plots of $WF_6(4\text{-}NC_5H_4R)$: a) R = H, b) R = CH_3, c) R = $N(CH_3)_2$. Thermal ellipsoids are drawn at the 50% probability level.

The dative W–N bonds are of equal length in the pyridine and 4-methylpyridine adducts, whereas that of $WF_6\{4\text{-}NC_5H_4N(CH_3)_2\}$ is slightly shorter and that of $WF_6(2\text{-}NC_5H_4F)$ [9] slightly longer (Table 3). The W–N bonds in these adducts are significantly shorter than the W–P bonds in analogous adducts with tertiary phosphines (2.564(1)–2.598(9) Å),[10] which is not surprising considering that phosphorus is larger than nitrogen. The trend in W–Pn (Pn = N, P) bond strengths is more directly compared by their normalised contacts;[23] the normalised W–N contact of $WF_6\{4\text{-}NC_5H_4N(CH_3)_2\}$ is the shortest (0.622), indicating that its W–Pn bond is the strongest of the series. Conversely, the 2-fluoropyridine (0.645) and tertiary phosphine (0.648–0.657) adducts possess longer normalised W–Pn contacts, reflecting weaker bonds.

Table 3. Selected Experimental and Calculated Bond Lengths (Å) and Normalised Contacts[a] in WF_6 and Its Adducts with Various Pnictogen (Pn) Bases

Base	W–F (average)		W–Pn			
	exptl	calcd[b]	exptl		calcd[b]	
—[c]	1.8264	1.845	—			
NC_5H_5	1.865	1.874	2.251(7)	[0.633]	2.343	[0.659]
4-$NC_5H_4CH_3$	1.864	1.875	2.250(3)	[0.633]	2.339	[0.658]
4-$NC_5H_4N(CH_3)_2$	1.8678	1.878	2.214(3)	[0.622]	2.301	[0.647]
4,4′-bipy[d]	—	1.874	—		2.351	[0.661]
2-NC_5H_4F[e]	1.84	1.865	2.294(9)	[0.645]	2.418	[0.680]
$P(CH_3)_3$[f]	1.86	—	2.598(9)	[0.657]	—	
$P(C_6H_5)(CH_3)_2$[f]	1.878	—	2.564(1)	[0.648]	—	
PH_3[f]	—	1.857	—		2.706	[0.761]

[a]Given in square brackets. Defined as the ratio of the bond length to the sum of the van der Waals radii (r) of the bonded atoms[23] (r(W) = 2.007[24]; r(P) = 1.95[25]; r(N) = 1.55[25]). [b]Calculated using the B3LYP functional with the Stuttgart basis set augmented by one f-type polarisation function (W; α_f = 0.823) and the aug-cc-pVTZ (H, C, N, F) basis set, unless otherwise noted. [c]Crystallographic bond lengths from reference 26. [d]Calculated using the B3LYP functional with the Stuttgart basis set augmented by one f-type polarisation function (W; α_f = 0.823) and the cc-pVTZ (H, C, N, F) basis set. θ = 89.9° [e]Crystallographic bond lengths from reference 9. [f]From reference 10.

The W–F bonds in WF_6(4-NC_5H_4R) (R = H, CH_3, $N(CH_3)_2$) and WF_6{$P(C_6H_5)(CH_3)_2$} are, on average, significantly elongated relative to crystalline WF_6 (1.8261(13)–1.8266(19) Å).[26] In the WF_6(4-$NC_5H_4CH_3$) adduct, the W−F(1) and W–F(2) bonds are longer than those of the fluorido ligands that form the capped face, but are predicted to be slightly shorter. The other adducts exhibit differences of lesser to no significance in crystallographic bond lengths. The contraction or elongation of the opposing and adjacent W–F bonds, respectively, is possibly a consequence of crystal packing.

As inferred from the adducts having crystallised in different space groups, the WF_6(4-NC_5H_4R) (R = H, CH_3, $N(CH_3)_2$) adducts exhibit highly dissimilar packing motifs despite their similar compositions and molecular structures. The WF_6(NC_5H_5) adduct crystallises such that the pyridyl ligands of adjacent molecules are π-stacked, which was also observed in the crystal

structure of the 2-fluoropyridine adduct.[9] However, in the former, adjacent pyridyl ligands are rotated 180° relative to one another (Fig. 2a) and in the latter, adjacent molecules are rotated approximately 120° relative to one another. Contrastingly, no such interactions occur in WF_6(4-$NC_5H_4CH_3$) (Fig. 2b), while in WF_6{4-$NC_5H_4N(CH_3)_2$}, the 4-(dimethylamino)pyridyl moieties overlap in such a way as to maximise stacking interactions between entirely delocalized π systems (Fig. 2c). Crystal packing diagrams are provided in the Supporting Information (Figs. S1–S3).

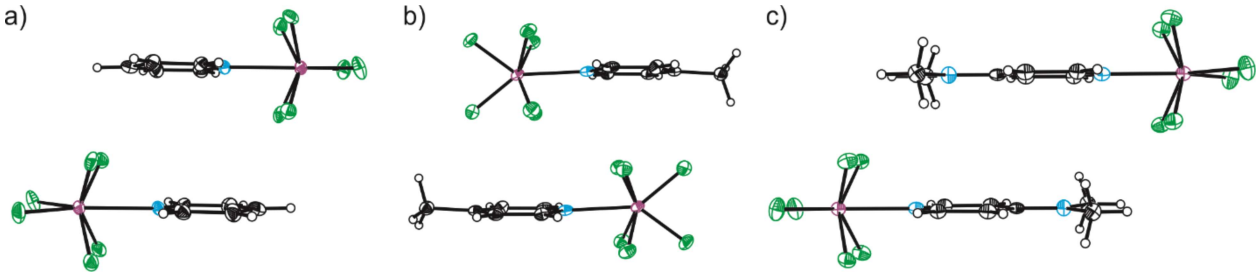

Fig. 2. Intermolecular π-stacking interactions in crystalline WF_6(4-NC_5H_4R): a) R = H, b) R = CH_3, c) R = $N(CH_3)_2$. Thermal ellipsoids are drawn at the 50% probability level.

Optimisation of the gas-phase geometries of WF_6(4-NC_5H_4R) (R = H, CH_3, $N(CH_3)_2$) and WF_6(2-NC_5H_4F) using the experimental geometries from the crystal structures as starting points resulted in C_{2v}- or C_s-symmetric structures, in excellent agreement with the experimental data, with the largest discrepancies being slight overestimations of the W–N bond lengths (Tables 1 and 2). As such, in the absence of crystallographic data, two gas-phase geometries were optimised for F_6W(4,4′-bipy)WF_6 as global (θ = 89.9°) and local (θ = 0.2°) energy minima with monocapped-trigonal-prismatic geometries at the tungsten centres, in which the planes of the two pyridyl rings intersect at an angle of 37.7–38.0° (Fig. 3). The W–F and W–N bonds in F_6W(4,4′-bipy)WF_6 appear similar in strength to those in the pyridine and 4-methylpyridine adducts. Atomic

coordinates and graphical representations of the optimised geometries are provided in the Supporting Information (Tables S5–S9 and Figs. S4–S8).

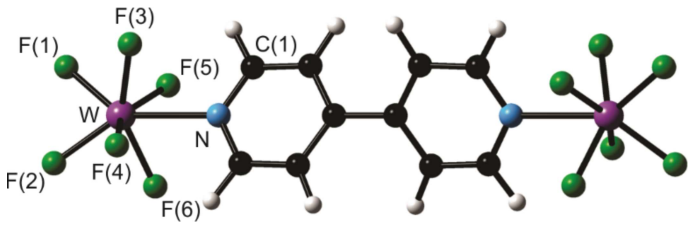

Fig. 3. Optimised gas-phase geometry of $F_6W(4,4'\text{-bipy})WF_6$ ($\theta = 0.2°$).

Given the different conformation of $WF_6(4\text{-}NC_5H_4CH_3)$ observed in its crystal structure, relaxed potential-energy-surface (PES) scans were conducted on $WF_6(NC_5H_5)$ and $WF_6(4\text{-}NC_5H_4CH_3)$ to ascertain the possible effect of the 4-methyl group on the overall geometry of the complex. In both cases, it was determined that the orthogonal configuration ($\theta = 90°$) observed in the crystal structure of $WF_6(4\text{-}NC_5H_4CH_3)$ was *ca*. 4 kJ mol^{-1} lower in energy than the co-planar configuration, with an overall energy barrier for rotation about the W–N bond of *ca*. 11 kJ mol^{-1} (Fig. 4). Thus, the presence of a methyl group in $WF_6(4\text{-}NC_5H_4CH_3)$ has no intrinsic effect on the energy of the adduct in regards to the preferred orientation of the pyridyl ligand, and such minute differences in energy could easily be overcome during crystal formation in favour of maximising packing efficiency.

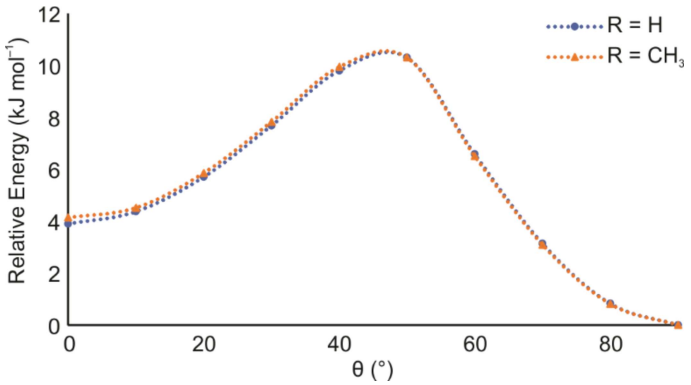

Fig. 4. Relaxed PES scans of the F(1)–W–N–C(1) dihedral angle (θ) in $WF_6(4\text{-}NC_5H_4R)$ (R = H, CH_3) from 0 to 90°.

Seeing that in $F_6W(4,4'\text{-bipy})WF_6$, the conformation of the pyridyl ligand does not cause any significant changes to other geometric properties of the adduct, further computational studies have been conducted based on those structures that best simulate their experimental counterparts. In the case of $F_6W(4,4'\text{-bipy})WF_6$, for which the actual geometry remains uncertain, the orthogonal conformation (θ = 89.9°) is discussed as it is, predictably, 8 kJ mol^{-1} lower in energy.

2.3. Raman Spectroscopy

The Raman spectrum of solid $WF_6(NC_5H_5)$ (Fig. 5a) is in excellent agreement with that reported previously.[8] The transfer of electron density from the pyridyl ligand to the tungsten centre causes weakening of the W–F bonds, accompanied by strengthening of the C–C and C–N bonds. Thus, bands corresponding to the pyridyl ligand tend to increase in frequency relative to those of free pyridine, while those corresponding to WF_6 decrease relative to free WF_6 (Table 4). The previous assignment of the symmetric W−F stretching mode to the band at 705 cm^{-1} [8] (vs. 771 cm^{-1} in free WF_6) is corroborated by frequency calculations. The band of the ring-breathing mode ($\nu_s(NC_5)$) has correspondingly shifted to 1024 cm^{-1} from 990 cm^{-1} in free pyridine. The

Raman spectra of the 4-methyl, 4-dimethylamino, and 2-fluoro[9] derivatives exhibit very similar general features to that of $WF_6(NC_5H_5)$ (Fig. 5 and Table 4).

The W–N stretching modes of adducts are assigned to bands that occur at *ca*. 150–200 cm^{-1}, which are higher in frequency than their predicted counterparts due to overestimation of the W–N bond lengths in the optimised geometries. The trend in frequencies of these bands does not correspond to the strength of the W–N bond, but rather the size of the pyridyl ligand. As such, the W–N stretching band in $WF_6\{4\text{-}NC_5H_4N(CH_3)_2\}$ is the lowest in frequency, despite it being predicted to possess the strongest W–N bond.

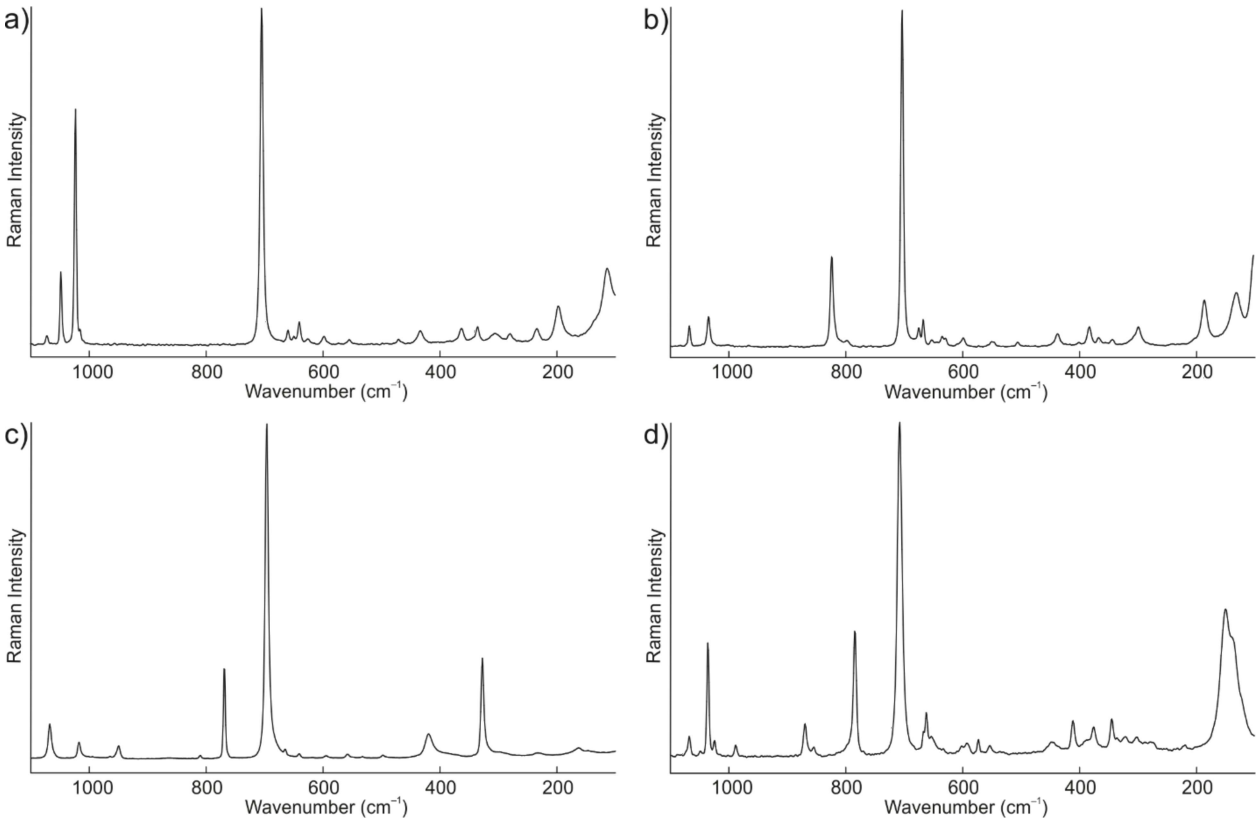

Fig. 5. Raman spectra of a) $WF_6(NC_5H_5)$, b) $WF_6(4\text{-}NC_5H_4CH_3)$, c) $WF_6\{4\text{-}NC_5H_4N(CH_3)_2\}$, and d) $F_6W(4,4'\text{-bipy})WF_6$. Spectra were recorded at ambient temperature.

Table 4. Experimental and Calculated[a] Frequencies (cm^{-1}) of Selected Vibrational Modes of WF_6 and Its Adducts with Various Nitrogen Bases

Base	$\nu_s(WF_6)$		$\nu_s(NC_5)$		$\nu(WN)$	
—	771	[755]	—		—	
NC_5H_5	705	[702]	1024	[1041]	198	[161]
4-$NC_5H_4CH_3$	704	[701]	1036	[1047]	185	[157]
4-$NC_5H_4N(CH_3)_2$	697	[696]	1018	[1039]	164	[140]
4,4′-bipy[b]	708	[700]	1037	[1050]	—	[154/65]
2-NC_5H_4F[c]	712	[709]	1029	[1080]	171	[126]

[a]Given in square brackets. Calculated using the B3LYP functional with the Stuttgart basis set augmented by one f-type polarisation function (W; $\alpha_f = 0.823$) and the aug-cc-pVTZ (H, C, N, F) basis set, unless otherwise noted. [b]Calculated using the B3LYP functional with the Stuttgart basis set augmented by one f-type polarisation function (W; $\alpha_f = 0.823$) and the cc-pVTZ (H, C, N, F) basis set. $\theta = 89.9°$. [c]Experimental data from reference 9.

The Raman spectrum of $F_6W(4,4'\text{-bipy})WF_6$ is much like those of the mononuclear adducts, suggesting a common geometry at the tungsten centres. This is further corroborated by the excellent agreement between the experimental and calculated Raman bands, though the calculated vibrational frequencies for the two conformations are too similar to deduce the true geometry of the adduct using vibrational spectroscopy (Table S14). The two $WF_6(NC_5H_4)$ moieties are predicted to be, in general, weakly vibrationally coupled such that splittings caused by symmetric and antisymmetric combinations of their vibrational modes could not be experimentally resolved. The symmetrically and antisymmetrically coupled W–N stretching modes are predicted to occur at *ca*. 60 and 150 cm^{-1}, respectively, but could not be positively identified in the experimental Raman spectrum, consistent with their low calculated intensities. Experimental and calculated vibrational frequencies, with assignments, for the adducts are detailed in the Supporting Information (Tables S11–S15).

3. Computational Results

The gas-phase geometries and vibrational frequencies of WF_6 and its adducts were calculated at the same levels of theory employed previously in computational studies of related imido- [18] and sulfidotungsten(VI) [27–29] complexes, with excellent agreement between experimental and calculated geometries and vibrational frequencies. As such, molecular orbitals were calculated and natural-bond-orbital (NBO) analyses were conducted.

3.1. Molecular Orbitals

The three degenerate LUMOs of WF_6 are comprised entirely of antibonding d_π-p_π interactions between the tungsten centre and fluorido ligands. In the adducts, the LUMOs retain this antibonding character, with additional σ*(W–N) interactions. The LUMOs of the adducts are significantly higher in energy than in free WF_6 (Table 5), which should serve to quench the sensitivity of WF_6 towards reduction.

Table 5. Selected MO Energies, HOMO-LUMO Gaps (ΔE), and Corresponding Absorption Wavelengths of WF_6 and Its Adducts with Various Nitrogen Bases[a]

Base	E_{MO} (eV)				ΔE (eV)	λ_{abs} (nm)[b]
	LUMO	HOMO	HOMO–1	HOMO–2		
—	–4.91					
NC_5H_5	–3.64	–8.56	–9.34	–9.75	4.92	252
4-$NC_5H_4CH_3$	–3.35	–8.68	–8.89	–9.95	5.33	232
4-$NC_5H_4N(CH_3)_2$	–3.26	–6.95	–8.17	–9.50	3.69	336
4,4′-bipy[c]	–4.08	–9.09	–9.11	–9.21	5.15	247
2-NC_5H_4F	–3.73	–8.44	–9.54	–9.98	4.71	263

[a]Calculated using the B3LYP functional with the Stuttgart basis set augmented by one f-type polarisation function (W; $\alpha_f = 0.823$) and the aug-cc-pVTZ (H, C, N, F) basis set, unless otherwise noted. [b]Predicted longest absorption wavelength based on the calculated HOMO-LUMO gaps. [c]Calculated using the B3LYP functional with the Stuttgart basis set augmented by one f-type polarisation function (W; $\alpha_f = 0.823$) and cc-pVTZ (H, C, N, F) basis set. θ = 89.9°.

The HOMOs and HOMOs–1 of the adducts are π-bonding in nature, with the electron density localised primarily on the pyridyl ligands, rendering the HOMO-LUMO transition a

ligand-to-metal charge transfer. This is readily apparent in the case of boldly coloured WF_6{4-$NC_5H_4N(CH_3)_2$}, for which the increase in the energy of the HOMO is brought on by the dimethylamino group causing a significant decrease of the HOMO-LUMO gap (Table 5). The d_σ-p_σ interactions that comprise the dative W–N bonds involve the d_{z^2} orbital on tungsten and are observed in the HOMOs–2. The W−F interactions in the HOMOs−2 are strongly antibonding in nature, corroborating the elongation of the W−F bonds upon adduct formation, though this is potentially exacerbated by steric crowding induced by a seventh ligand. These characteristic MOs have been visualised for $WF_6(NC_5H_5)$ (Fig. 6) and their compositions are very similar to those of the other adducts.

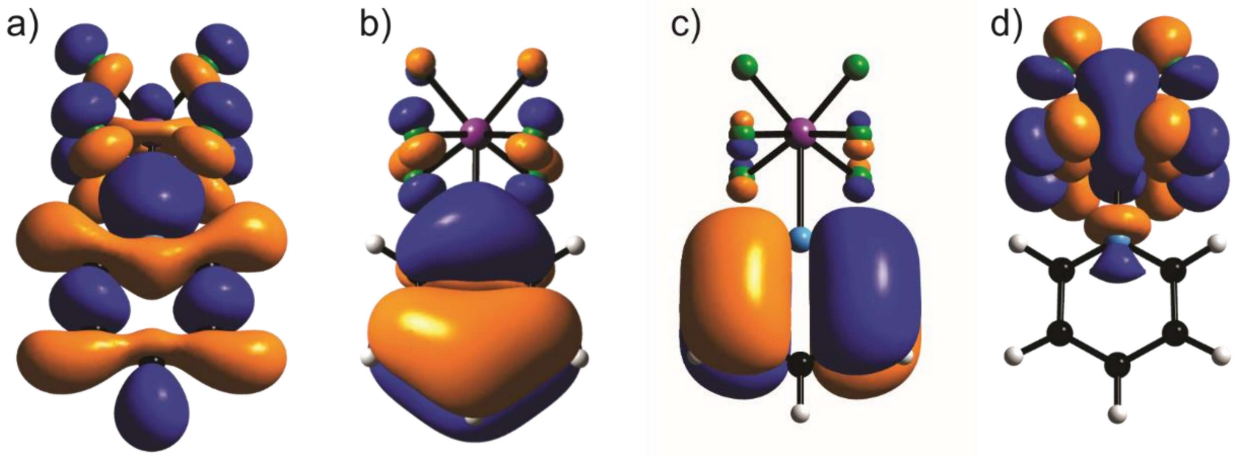

Fig. 6. Selected MOs of $WF_6(NC_5H_5)$: a) HOMO–2, b) HOMO–1, c) HOMO, d) LUMO. Isosurfaces are drawn at 0.02 e $Å^{-3}$.

3.2. NBO Analyses

Upon coordination of the nitrogen base to the tungsten centre, the natural-population-analysis (NPA) charge of the tungsten centre in the mononuclear adducts decreases slightly in comparison to that in free WF_6 (Table 6). This coincides with a slight decrease in the Wiberg bond

indices (WBIs) of the W−F bonds, more prevalently in those adjacent to (0.71−0.72) than opposite (0.75−0.77) the pyridyl ligand. The dative W−N bonds (WBI: 0.31−0.40) are approximately half as strong as the W−F bonds, indicating significant covalent character, with that of the 2-fluoropyridine adduct being the weakest. Surprisingly, the same WBI was calculated for the W–N bonds of the 4-methylpyridine and 4-(dimethylamino)pyridine adducts, despite the stronger W–N bond in the latter, as well as the difference in Lewis basicities of the parent nitrogen bases. The atomic charges and WBIs of $F_6W(4,4'\text{-bipy})WF_6$ are of a similar magnitude to those of the mononuclear adducts, and differences between the two conformations are effectively indiscernible. Complete NPA charges, Wiberg valences, and WBIs involving non-hydrogen atoms are provided in the Supporting Information (Tables S16–S17).

Table 6. Selected NPA Charges and WBIs for WF_6 and Its Adducts with Various Nitrogen Bases[a]

Base	Charge (W)	WBI	
		W–F	W–N
—	+2.80	0.78	—
NC_5H_5	+2.74	0.72–0.76	0.36
4-$NC_5H_4CH_3$	+2.74	0.71–0.75	0.40
4-$NC_5H_4N(CH_3)_2$	+2.74	0.71–0.75	0.40
4,4′-bipy[b]	+2.66	0.73–0.77	0.39
2-NC_5H_4F	+2.76	0.71–0.77	0.31

[a]Calculated using the B3LYP functional with the Stuttgart basis set augmented by one f-type polarisation function (W; $\alpha_f = 0.823$) and the aug-cc-pVTZ (H, C, N, F) basis set, unless otherwise noted. [b]Calculated using the B3LYP functional with the Stuttgart basis set augmented by one f-type polarisation function (W; $\alpha_f = 0.823$) and the cc-pVTZ (H, C, N, F) basis set. $\theta = 89.9°$. The lower charge on W is a consequence of the cc-pVTZ basis set (see Table S21 for a comparison of the results for $WF_6(NC_5H_5)$ with the *aug*-cc-pVTZ and cc-pVTZ basis sets).

4. Conclusions

The Lewis-acid behaviour of WF_6 towards pyridine and several derivatives thereof has been investigated systematically. The capped-trigonal-prismatic geometries of the mononuclear adducts have been elucidated by low-temperature X-ray crystallography, and a combination of Raman spectroscopic and computational studies has been employed to suggest this geometry for the dinuclear $F_6W(4,4'\text{-bipy})WF_6$ adduct. The crystal structures revealed two distinct conformations, which represent the two minima on the potential energy surface with small calculated energy differences (4 kJ mol^{-1} for $WF_6(NC_5H_5)$) that describe the rotation of the pyridyl ligand with respect to the WF_6 trigonal prism. Bonding in the adducts was explored via molecular-orbital calculations and NBO analyses, which established that the dative W–N bonds, though weak, are largely covalent in nature.

5. Experimental

5.1. Materials and Apparatus

All reactions were carried out in heat-sealed ¼”-o.d. FEP reactors which were connected to either stainless-steel or Kel-F valves via flared fittings and passivated with 100% F_2. Volatile materials were distilled on a Pyrex vacuum line equipped with glass valves fitted with 6-mm o.d. PTFE J. Young stopcocks, with the exception of WF_6, which was distilled through a nickel/316 stainless-steel vacuum line equipped with 316 stainless-steel valves (Autoclave Engineers) and pre-passivated with 100% F_2. Solid materials were handled in a dry box (Omni Lab, Vacuum Atmospheres) under an atmosphere of dry N_2.

Acetonitrile (Baker, 99.8%) was dried according to the literature method.[30] Sulfur dioxide (Matheson) and pyridine (Sigma-Aldrich, 99.8%) were dried over CaH_2. 4-Methylpyridine was dried over potassium and distilled onto freshly activated 4-Å molecular sieves. Tungsten

hexafluoride (Ozark-Mahoning), 4-(dimethylamino)pyridine (Sigma-Aldrich, 99%), and 4,4′-bipyridine (Sigma-Aldrich, 98%) were used as provided. **Note:** *Concentrated solutions of pyridine and derivatives thereof in CH_2Cl_2 were kept cold (*ca. –50 °*C), as they have been found to react slowly at ambient temperature to afford* N,N′*-methylenebispyridinium salts*.[31]

5.2. Syntheses

5.2.1. $WF_6(NC_5H_5)$

The $WF_6(NC_5H_5)$ adduct was prepared as described previously.[8] $\delta(^{19}F)$ (ppm): 166 (s, br). $\delta(^{1}H)$ (ppm): 9.08 (H_o, dd, $^{3}J(H_o–H_m) = 6.6$ Hz, $^{4}J(H_o–H_p) = 1.4$ Hz); 8.29 (H_p, tt, $^{3}J(H_p–H_m) = 7.6$ Hz); 7.82 (H_m, dd). $\delta(^{13}C\{^{1}H\})$ (ppm): 145.84 (C_o), 144.12 (C_p), 127.32 (C_m).

5.2.2. $WF_6(4\text{-}NC_5H_4CH_3)$

4-Methylpyridine (0.064 g, 0.69 mmol) and CH_2Cl_2 (0.695 g) were distilled into a ¼”-o.d. FEP reactor at −196 °C, after which the reactor was kept below –50 °C. Subsequently, WF_6 (0.280 g, 0.940 mmol) was distilled into the reactor at −196 °C and the mixture was warmed to –50 °C, upon which a white solid immediately precipitated from solution. The reactor was allowed to warm further to ambient temperature, resulting in dissolution of the solid to afford a colourless solution. The volatile materials were removed under dynamic vacuum at −60 °C for 1 h and at ambient temperature for 10 min, affording $WF_6(4\text{-}NC_5H_4CH_3)$ (0.251 g, 0.642 mmol, 93% with respect to 4-methylpyridine) as a white powder. $\delta(^{19}F)$ (ppm): 168 (s, br). $\delta(^{1}H)$ (ppm): 8.98 (H_o, d, $^{3}J(^{1}H_o–^{1}H_m) = 7.7$ Hz); 7.61 (H_m, d); 2.49 (CH_3, s). $\delta(^{13}C\{^{1}H\})$ (ppm): 145.58 (C_o), 127.66 (C_m), 21.35 (CH_3). Impurities of $[WF_7]^-$ (3 mol%, $\delta(^{19}F) = 143.42$ ppm) and various oxidotungsten(VI) species (trace, $\delta(^{19}F) = 61–78$ ppm) were observed by ^{19}F NMR spectroscopy.

5.2.3. $WF_6\{4\text{-}NC_5H_4N(CH_3)_2\}$

In the dry box, a ¼"-o.d. FEP reactor was charged with 4-(dimethylamino)pyridine (0.060 g, 0.49 mmol). Dichloromethane (0.767 g) was distilled into the reactor at −196 °C, followed by WF_6 (0.179 g, 0.601 mmol). Upon warming the reactor to −60 °C, a dark red suspension formed immediately. The reactor was warmed to ambient temperature, then briefly to 45 °C, with agitation to ensure reaction completion. The volatile materials were removed under dynamic vacuum at −70 °C for 2 h and at ambient temperature for 5 min, affording $WF_6\{4\text{-}NC_5H_4N(CH_3)_2\}$ (0.208 g, 0.495 mmol, 100% yield with respect to 4-(dimethylamino)pyridine) as a dark red powder. $\delta(^{19}F)$ (ppm): 164 (s, br). $\delta(^{1}H)$ (ppm): 8.58 (H_o, d, $^{3}J(^{1}H_o-^{1}H_m)$ = 7.7 Hz); 6.68 (H_m, d); 3.10 (CH_3, s). $\delta(^{13}C\{^{1}H\})$ (ppm): 145.61 (C_o), 106.74 (C_m), 39.88 (CH_3). Impurities of $[WF_7]^-$ (6 mol%, $\delta(^{19}F)$ = 143.55 ppm) and $WOF_4\{4\text{-}NC_5H_4N(CH_3)_2\}$ (trace, $\delta(^{19}F)$ = 61.09 ppm, $^{1}J(^{19}F-^{183}W)$ = 63.5 Hz) were observed by ^{19}F NMR spectroscopy.

5.2.4. $F_6W(4,4'\text{-bipy})WF_6$

In the dry box, a ¼"-o.d. FEP reactor was charged with 4,4′-bipyridine (0.029 g, 0.19 mmol). Dichloromethane (0.415 g) was distilled into the reactor at –196 °C, followed by WF_6 (0.231 g, 0.776 mmol). Upon warming the reactor to ambient temperature, a large amount of white solid precipitated from the solution; brief heating to 45 °C or agitation in an ultrasonic bath did not effect any noticeable dissolution. The reactor was left to stand at ambient temperature for 2 h with occasional agitation before the volatile materials were removed under dynamic vacuum at –70 °C for 30 min and at ambient temperature for 2 min, affording $F_6W(4,4'\text{-bipy})WF_6$ (0.141 g, 0.188 mmol, 100% yield with respect to 4,4′-bipyridine) as a white powder. The sample could not be characterised by ^{19}F NMR spectroscopy due to its insolubility in the solvents employed herein.

5.3. X-ray Crystallography

5.3.1. Crystal Growth and Mounting

Colourless plates of $WF_6(NC_5H_5)$ crystallised from CH_3CN in a ¼"-o.d. FEP reactor upon cooling the bottom of the reactor to −196 °C to effect rapid crystallisation of a small amount of the solute, followed by submerging the reactor in an ethanol bath cooled to −10 °C and slowly cooling to −40 °C thereafter. Colourless blocks of $WF_6(4\text{-}NC_5H_4CH_3)$ could be crystallised by slowly cooling a concentrated SO_2 solution to −70 °C, which also served as an alternative method of crystallisation for $WF_6(NC_5H_5)$. Red-orange needles of $WF_6\{4\text{-}NC_5H_4N(CH_3)_2\}$ were grown at −40 °C from a dilute CH_3CN solution over 1 h. After removal of the solvent under dynamic vacuum, the reactors were cut on an aluminum trough cooled to −80 °C by a stream of dry N_2, which was generated by passing the gas through a Dewar of liquid N_2, and the crystals were deposited onto the trough. The selected crystals were affixed to a Nylon cryo-loop coated in perfluorinated polyether oil (Fomblin Z-25) and quickly transferred to the goniometer using liquid-nitrogen-cooled cryotongs.

5.3.2. Data Collection and Reduction

The crystals were centered on a Rigaku SuperNova diffractometer equipped with a Dectris Pilatus 3R 200K-A hybrid-pixel-array detector, a four-circle κ goniometer, an Oxford Cryostream 800, and sealed MoK_α and CuK_α X-ray sources. Data were collected using the MoK_α source (λ = 0.71073 Å) at −173 °C. Crystals were screened for quality before a pre-experiment was run to determine the unit cell, and a data-collection strategy was calculated based on the determined unit cell and intensity of the preliminary data. This strategy was optimised to collect five-fold redundant data at a resolution of 0.77 Å. The data were processed using CrysAlisPro,[32] which applied necessary Lorentz and polarisation corrections to the integrated data and scaled the data. A numerical (analytic) absorption correction was generated based upon the indexed faces of the

crystal. In the case of $WF_6(NC_5H_5)$, upon reduction of the data, frames with a $R_{int} > 0.2$ were omitted, which did not adversely affect the completeness of the data.

5.3.3. Structure Solution and Refinement

Atom positions were determined using the intrinsic phasing method (ShelXT[33]) and were refined using least-squares refinement (ShelXL[34]). Non-hydrogen atoms were refined anisotropically and recommended weights for the atoms were determined before hydrogen atoms were introduced using a riding model (HFIX). The maximum and minimum electron density in the Fourier difference maps were located near the tungsten atom in all cases. Structure solution and refinement were performed with the aid of Olex2 (version 1.2).[35] CCDC deposition numbers: 1853269 ($WF_6(NC_5H_5)$), 1853270 ($WF_6(4\text{-}NC_5H_4CH_3)$), 1853271 ($WF_6\{4\text{-}NC_5H_4N(CH_3)_2\}$).

5.4. Raman Spectroscopy

All Raman spectra were recorded on solid samples in flame-sealed glass melting point capillaries at ambient temperature using a Bruker RFS-100 Raman spectrometer outfitted with a quartz beam-splitter and liquid-N_2-cooled germanium detector. The 1064-nm line of a Nd:YAG laser was used for excitation of the sample, and back-scattered (180°) radiation was sampled. The usable Stokes range of the collected data was 85 to 3500 cm^{-1} with a spectral resolution of 2 cm^{-1}. The laser power was set to 200 mW.

5.5. NMR Spectroscopy

All NMR spectra were recorded in heat-sealed 4-mm o.d. FEP tubes in 5-mm o.d. glass inserts using a Bruker Avance II 300 MHz spectrometer equipped with a 5-mm broadband probe. Spectra were recorded unlocked on dilute CH_3CN solutions at 20°C, and referenced externally to $CFCl_3$ (^{19}F) and $Si(CH_3)_4$ (^1H and $^{13}C\{^1H\}$) at 20 °C.

5.6. Computational Details

All DFT calculations were performed in the gas phase using the B3LYP functional, as implemented in Gaussian 09 (revision D.01).[36] The Stuttgart basis set augmented by one f-type polarisation function ($\alpha_f = 0.823$),[37] and the associated pseudopotentials were used for tungsten. The aug-cc-pVTZ basis set was used for hydrogen, carbon, nitrogen, and fluorine in all cases except $F_6W(4,4'\text{-bipy})WF_6$, for which the cc-pVTZ basis set was used instead. For comparative purposes, geometry optimisations, vibrational frequency calculations, and NBO analyses were performed for $WF_6(NC_5H_5)$ with and without diffuse functions on hydrogen, nitrogen, carbon, and fluorine, showing no significant differences in the salient values. The largest disparity is seen in the NPA charge of tungsten, which needs to be considered when comparing the charges on tungsten in $F_6W(4,4'\text{-bipy})WF_6$ with those in the other adducts. See the Supporting Information (Tables S19–S21) for such comparisons. Basis set parameters were obtained from the EMSL Basis Set Exchange.[38,39] Geometry optimisations were performed using analytic gradient methods, and all subsequent calculations were performed using the optimised geometries. Whenever possible, the experimental geometries were used as starting points for the geometry optimisations. The NBO analyses were performed using NBO (version 6.0)[40], and GaussView (version 5.0)[41] was used to visualised the vibrational modes and to aid in their description.

Acknowledgements

We would like to thank the Natural Sciences and Engineering Research Council of Canada (M.G. and S.D.W.: Discovery grants; D.T.: CGS-M and PGS-D scholarships) and the University of Lethbridge for supporting this work. We would also like to thank the university for awarding the SGS Dean's Scholarship and Tuition Award to D.T. The computational studies were performed

using equipment funded through the Canada Foundation of Innovation, as well as resources made available through Westgrid and Compute/Calcul Canada.

References

(1) R. Craciun, D. Picone, R.T. Long, S. Li, D.A. Dixon, K.A. Peterson, K.O. Christe, Third row transition metal hexafluorides, extraordinary oxidizers, and Lewis acids: electron affinities, fluoride affinities, and heats of formation of WF_6, ReF_6, OsF_6, IrF_6, PtF_6, and AuF_6[†], Inorg. Chem. 49 (2010) 1056–1070.

(2) R. Craciun, R.T. Long, D.A. Dixon, K.O. Christe, Electron affinities, fluoride affinities, and heats of formation of the second row transition metal hexafluorides: MF_6 (M = Mo, Tc, Ru, Rh, Pd, Ag), J. Phys. Chem. A. 114 (2010) 7571–7582.

(3) K.O. Christe, D.A. Dixon, D. McLemore, W.W. Wilson, J.A. Sheehy, J.A. Boatz, On a quantitative scale for Lewis acidity and recent progress in polynitrogen chemistry, J. Fluorine Chem. 101 (2000) 151–153.

(4) M.J. Molski, K. Seppelt, The transition metal hexafluorides, Dalton Trans. (2009) 3379.

(5) K. Seppelt, Molecular Hexafluorides, Chem. Rev. 115 (2015) 1296–1306.

(6) F.N. Tebbe, E.L. Muetterties, Further evidence of stereochemical nonrigidity in five- and seven-coordinate structures, Inorg. Chem. 7 (1968) 172–174.

(7) A. Steigel, S. Brownstein, Fluorine exchange in complexes of tungsten hexafluoride, J. Am. Chem. Soc. 96 (1974) 6227.

(8) L. Arnaudet, R. Bougon, B. Buu, M. Lance, M. Nierlich, P. Thuéry, J. Vigner, Characterization of the adducts WF_6·py and WF_6·2py (py = pyridine): crystal structure of WF_6·2py, J. Fluorine Chem. 71 (1995) 123–129.

(9) L. Arnaudet, R. Bougon, B. Ban, M. Lance, M. Nierlich, J. Vigner, Preparation, characterization, and crystal structure of the tungsten hexafluoride and tetrafluoride oxide

adducts WF_6·F-py and WOF_4·F-py (F-py = 2-fluoropyridine), Inorg. Chem. 32 (1993) 1142–1146.

(10) S. El-Kurdi, A.-A. Al-Terkawi, B. Schmidt, A. Dimitrov, K. Seppelt, Tungsten(VI) and tungsten(V) fluoride complexes, Chem. Eur. J. 16 (2010) 595–599.

(11) S. Giese, K. Seppelt, Structural principles in seven-coordinate subgroup compounds: the complex anions MoF_7^-, WF_7^-, and $ReOF_6^-$, Angew. Chem. Int. Ed. Engl. 33 (1994) 461–463.

(12) A. Dimitrov, S. Seidel, K. Seppelt, Substituted tungsten fluorides, Eur. J. Inorg. Chem. 1999 (1999) 95–99.

(13) L. Arnaudet, R. Bougon, B. Ban, M. Lance, A. Navaza, M. Nierlich, J. Vigner, 2,2′-Bipyridyl fluoro complexes of tungsten(VI): preparation, characterization and crystal structure of $[WF_4(bipy)_2]^{2+}\cdot 2[WF_7]^-\cdot WF_6$ and $[WF4(bipy)_2]^{2+}\cdot 2[WF_7]^-\cdot CH_3CN$; preparation and characterization of WF_6·bipy, J. Fluorine Chem. 67 (1994) 17–25.

(14) L. Arnaudet, R. Bougon, B. Ban, P. Charpin, J. Isabey, M. Lance, M. Nierlich, J. Vigner, 2,2′-Bipyridyl adducts of tungsten oxide fluorides: preparation and characterization of WOF_4·bipy and WO_2F_2·bipy; crystal structure of WO_2F_2·bipy, Can. J. Chem. 68 (1990) 507–512.

(15) L. Arnaudet, R. Bougon, B. Ban, M. Lance, A. Navaza, M. Nierlich, J. Vigner, Structure of the new fluoro complex of tungsten(VI): $[WF_4(bipy)_2]^{2+}\cdot 2[W_2O_2F_9]^-\cdot 0.25HF$ (bipy = 2,2′-bipyridyl), J. Fluorine Chem. 59 (1992) 141–152.

(16) W.W. Wilson, K.O. Christe, $NF_4^+WF_7^-$ and $NF_4^+UF_7^-$ and methods of preparation, 1982.

(17) K. Matsumoto, R. Hagiwara, R. Yoshida, Y. Ito, Z. Mazej, P. Benkič, B. Žemva, O. Tamada, H. Yoshino, S. Matsubara, Syntheses, structures and properties of 1-ethyl-3-methylimidazolium salts of fluorocomplex anions, Dalton Trans. (2004) 144–149.

(18) D. Turnbull, S.D. Wetmore, M. Gerken, Syntheses and characterization of $W(NC_6F_5)F_5^-$ and $W_2(NC_6F_5)_2F_9^-$ salts and computational studies of the $W(NR)F_5^-$ (R = H, F, CH_3, CF_3, C_6H_5, C_6F_5) anions, Inorg. Chem. 56 (2017) 12581–12593.

(19) C.J. Barbour, J.H. Cameron, J.M. Winfield, Preparation of the solvated iron(II) cation in acetonitrile using high oxidation-state fluorides and its reaction with trimethyl phosphite, J. Chem. Soc. Dalton Trans. (1980) 2001–2005.

(20) N. Bao, J.M. Winfield, Oxidation of molybdenum and tungsten metals by molybdenum and tungsten hexafluorides in acetonitrile. Preparation of the 1:1 pentafluoride acetonitrile complexes, J. Fluorine Chem. 50 (1990) 339–343.

(21) W.W. Wilson, K.O. Christe, Perfluoroammonium and cesium fluorotungstates, Inorg. Chem. 20 (1981) 4139–4143.

(22) C. Laurence, J.-F. Gal, Lewis basicity and affinity scales: data and measurement, John Wiley (2010) pg. 91–92.

(23) P. Scilabra, G. Terraneo, G. Resnati, Fluorinated elements of group 15 as pnictogen bond donor sites, J. Fluorine Chem. 203 (2017) 62–74.

(24) S.S. Batsanov, Calculation of van der Waals radii of atoms from bond distances, J. Mol. Struct. 468 (1999) 151–159.

(25) A. Bondi, van der Waals volumes and radii, J. Phys. Chem. 68 (1964) 441–451.

(26) T. Drews, J. Supeł, A. Hagenbach, K. Seppelt, Solid state molecular structures of transition metal hexafluorides, Inorg. Chem. 45 (2006) 3782–3788.

(27) J. Nieboer, W. Hillary, X. Yu, H.P.A. Mercier, M. Gerken, Syntheses, characterization, and computational study of WSF_4 and $WSF_4 \cdot CH_3CN$, Inorg. Chem. 48 (2009) 11251–11258.

(28) J. Nieboer, X. Yu, P. Chaudhary, H.P.A. Mercier, M. Gerken, Synthesis, characterization, and computational study of $WSF_4 \cdot NC_5H_5$, Z. Anorg. Allg. Chem. 638 (2012) 520–525.

(29) J. Nieboer, R. Haiges, W. Hillary, X. Yu, T. Richardet, H.P.A. Mercier, M. Gerken, Fluoride-ion acceptor properties of WSF_4: Synthesis, charcaterization, and computational study of the WSF_5^- and $W_2S_2F_9^-$ anions and ^{19}F NMR spectroscopic characterization of the $W_2OSF_9^-$ anion, Inorg. Chem. 51 (2012) 6350–6359.

(30) J.M. Winfield, Acetonitrile, a convenient solvent for inorganic fluorides, J. Fluorine Chem. 25 (1984) 91–98.

(31) A.B. Rudine, M.G. Walter, C.C. Wamser, Reaction of dichloromethane with pyridine derivatives under ambient conditions, J. Org. Chem. 75 (2010) 4292–4295.

(32) CrysAlisPro, Agilent Technologies, Ltd., Yarnton, Oxfordshire, England, 2014.

(33) G. M. Sheldrick, SHELXT, University of Göttingen, Göttingen, Germany, 2015.

(34) G. M. Sheldrick, SHELXL, University of Göttingen, Göttingen, Germany, 2015.

(35) O. V. Dolomanov, L. J. Bourhis, R. J. Gildea, J. A. K. Howard, H. Puschmann, Olex2, version 1.2, OlexSys Ltd., Durham University, U.K. 2017.

(36) M. J. Frisch, G. W. Trucks, H. B. Schlegel, G. E. Scuseria, M. A. Robb, J. R. Cheeseman, G. Scalmani, V. Barone, G. A. Petersson, H. Nakatsuji, X. Li, M. Caricato, A. Marenich, J. Bloino, B. G. Janesko, R. Gomperts, B. Mennucci, H. P. Hratchian, J. V. Ortiz, A. F. Izmaylov, J. L. Sonnenberg, D. Williams-Young, F. Ding, F. Lipparini, F. Egidi, J. Goings, B. Peng, A. Petrone, T. Henderson, D. Ranasinghe, V. G. Zakrzewski, J. Gao, N. Rega, G.

Zheng, W. Liang, M. Hada, M. Ehara, K. Toyota, R. Fukuda, J. Hasegawa, M. Ishida, T. Nakajima, Y. Honda, O. Kitao, H. Nakai, T. Vreven, K. Throssell, J. A. Montgomery, Jr., J. E. Peralta, F. Ogliaro, M. Bearpark, J. J. Heyd, E. Brothers, K. N. Kudin, V. N. Staroverov, T. Keith, R. Kobayashi, J. Normand, K. Raghavachari, A. Rendell, J. C. Burant, S. S. Iyengar, J. Tomasi, M. Cossi, J. M. Millam, M. Klene, C. Adamo, R. Cammi, J. W. Ochterski, R. L. Martin, K. Morokuma, O. Farkas, J. B. Foresman, and D. J. Fox, Gaussian 09, revision D.01, Gaussian, Inc., Wallingford CT, 2016.

(37) A.W. Ehlers, M. Böhme, S. Dapprich, A. Gobbi, A. Höllwarth, V. Jonas, K.F. Köhler, R. Stegmann, A. Veldkamp, G. Frenking, A set of f-polarization functions for pseudo-potential basis sets of the transition metals Sc-Cu, Y-Ag and La-Au, Chem. Phys. Lett. 208 (1993) 111–114.

(38) D. Feller, The role of databases in support of computational chemistry calculations, J. Comput. Chem. 17 (1996) 1571–1586.

(39) K.L. Schuchardt, B.T. Didier, T. Elsethagen, L. Sun, V. Gurumoorthi, J. Chase, J. Li, T.L. Windus, Basis Set Exchange: A community database for computational sciences, J. Chem. Inf. Model. 47 (2007) 1045–1052.

(40) E.D. Glendening, J.K. Badenhoop, A.E. Reed, J.E. Carpenter, J.A. Bohmann, C.M. Morales, C.R. Landis, F. Weinhold, NBO 6.0, Theoretical Chemistry Institute: University of Wisconsin, Madison, 2013.

(41) GaussView, version 5.0, Gaussian, Inc., Wallingford, CT, 2016.